International Communications in Heat and Mass Transfer 146 (2023) 106900

Contents lists available at ScienceDirect

International Communications in Heat and Mass Transfer

journal homepage: www.elsevier.com/locate/ichmt

Structural parameter design of welded plate heat exchanger based on multi-objective optimization algorithm

Li Yicong, Shi Chunyu, Liu Wei, Liu Zhichun *

School of Energy and Power Engineering, Huazhong University of Science and Technology, Wuhan 430074, China

ARTICLE INFO

Keywords:
Structural optimization
Welded plate heat exchanger
Artificial neural network
Multi-objective optimization

ABSTRACT

A numerical investigation was conducted to explore the heat transfer and flow characteristics of welded plate heat exchanger with chevron sinusoidal corrugated plates and to find the optimal parameter design in this paper. For better thermo-hydraulic performance, the effects of chevron angle (β = *30°,45°,60°*), the height of the corrugations (H = *3,5,7,9*) and the pitch of corrugations (P = *15,20,30,45,60*) were studied with inlet velocity ranged from 0.1 m/s to 0.5 m/s. Moreover, artificial neural networks (ANNs) and multi-objective genetic algorithm (MOGA) were employed to obtain optimization solutions of the structural parameters. With the analysis of flow form inside the flow channel, it was proposed that the chevron sinusoidal corrugated plates were helpful to transform the axial velocity of fluid to radial velocity, forming turbulence and secondary flow in the narrow region. The numerical results showed that the comprehensive performance of the plate with $\beta = 45°$ was better than the other two, while $P = 30$ mm and $H = 9$ mm also performed well in this paper. Besides, an optimal parameters set was obtained with $P = 15.132$ mm, $H = 3.005$ mm, $\beta = 45.495°$ when the velocity of inlet was set as 0.1 m/s, the maximum *JF* could reach 0.034 as the results of multi-objective optimization.

1. Introduction

Plate heat exchanger (PHE) was used as heat transfer equipment to achieve the heat exchange of cold and hot fluids. It had the advantages of low resistance coefficient, efficient utilization, low operating costs and so on [2]. It was widely used in aerospace, petrochemical, refrigeration and low-temperature industries, and played a big role in industrial production. Welded plate heat exchanger (WPHE), as a special type of plate heat exchanger with a special structure, was a new type of high-efficiency heat exchanger made of a series of metal sheets with certain corrugated shapes stacked and welded. Compared with the conventional heat exchangers, its heat transfer coefficient was much higher under the same working conditions, and it tended to replace the conventional heat exchangers within the scope of application [3].

As the core heat transfer component of the PHE, the number and structural size of corrugated plates highly affected the thermal performance of the PHE. At present, many experts and scholars had conducted relevant research on the heat transfer and flow characteristic of PHE, mainly using experimental and numerical methods [4–8]. In terms of experiments, W.W.Focke [9] measured the variation of *Nu* and *f* with the chevron angle through experiments, and obtained the variation of the flow form in the flow channel. When the chevron angle was less than 60°, the flow form was "cross flow" while the chevron angle was greater than 60°, the flow form was "zigzag flow". With that, Dovic, Zimmer [11] and others used visual experimental methods to explore single-phase flow in a chevron sinusoidal corrugated plate. The results showed that the mechanism of flow form Changing with chevron angle obtained was consistent with the conclusion studied by W.W.Focke through experiments, and it was found that there are two types of flow forms in the flow channel; When the chevron angle was less than 60°, the flow form was a "cross flow" flowing along the groove. If the chevron angle was greater than 60°, the flow form would translate to a "zigzag flow" that turned back at the contact surface of the corrugated plates. Rush [12] carried out an experimental study on fluids in laminar and transitional flow in the sinusoidal corrugated channel. It could be concluded that the geometric parameters of the sinusoidal corrugated channel and the Reynolds number were the main factors affecting the position where the fluid began to mix. The fluid would always reach unstable flow at the outlet under low *Re*. With the increase of Reynolds number, this unstable flow developed towards the inlet. Muley et al. [13] had studied the effects of chevron angle and corrugated area expansion coefficient on heat transfer and flow resistance of PHE through experiments, and took them into account in the fitted

* Corresponding author.
E-mail address: zcliu@hust.edu.cn (L. Zhichun).

https://doi.org/10.1016/j.icheatmasstransfer.2023.106900

Nomenclature

A_{ht}	The area of heated wall (m^2)
c	The heat capacity of working fluid ($J/kg \bullet K^{-1}$)
D	The hydraulic diameter (mm)
f	The friction factors
g	The mass flow of working fluid (kg/s)
h	The heat transfer coefficient ($W/m^2 \bullet K$)
I	The turbulence intensity
JF	The performance evaluation
k	Turbulent kinetic energy (m^2s^{-2})
L	The length of flow direction (m)
Nu	The Nusselt number
P	Pressure (Pa)
Pr	Prandtl number
Q	The total rate of heat transfer (w)
Re	The Reynolds number
t_{out}	The temperature of the outlet (K)
t_{in}	The temperature of the inlet (K)
T_{wall}	The temperature of wall (K)
T	Temperature of the working fluid (K)
u_{in}	The velocity of working fluid (m/s)
V	Volume of working fluid (m^3)
W	The width of plate (m)

Greek symbols

ΔP	The pressure drops between the inlet and outlet (Pa)
Δt_m	The temperature difference (K)
ε	Dissipation rate of turbulent kinetic energy of the k- ε model (m^2s^{-3})
λ	Thermal conductivity ($W/m \bullet K^{-1}$)
μ	Dynamic viscosity ($kg/m \bullet s^{-1}$)
ν	Kinematic viscosity ($m^2 \bullet s^{-1}$)
ρ	Density of working fluid (kg/m^3)

Subscripts

in	Inlet
out	Outlet
T	Turbulence
wall	Wall

correlation between heat transfer and flow resistance. Sang Dong Hwang [14] studied the flow form in the corrugated channel through experiments, and found that the fluid produced a secondary flow perpendicular to the main flow in the corrugated channel when the Reynolds number was low, and the pattern of the secondary flow was observed. Furthermore, D. Dovic [15] had experimentally studied the variation of turbulence intensity in the corrugated plate channel with chevron angle. The research showed that when the Reynolds number was low, the fluid in the channel with larger chevron angle was more likely to reach the turbulent state.

Although experimental data could accurately infer the thermo-hydraulics of PHE, but experimental research was limited by the construction of experimental platforms, making it difficult for researchers to observe the flow of fluid throughout the entire flow field. With the advancement of computational technology and simulation methods, CFD had become a complementary tool with experiments, used by many experts and scholars, and gradually occupying a place in the scientific research. Due to the fact that CFD technology could help researchers save time, reduced experimental costs, and make up for the shortcomings of limited sampling points and positions , many scholars had also used CFD for research in recent years. Han [16] simulated the single-phase laminar flow of highly viscous fluid in the adjacent dual channels (including inlet and outlet sections) of a chevron sinusoidal corrugated plate using CFD technology, and obtained the distributions of velocity, temperature and pressure fields in the flow channel. The difference between the high velocity zone and the low velocity zone in the groove was obvious; The temperature gradient near the contact point of the corrugated plate was larger than that of the middle area while the heat transfer coefficient at the contact point was the highest. Ilian G et al. [17] used CFD technology to numerically simulate the laminar and turbulent flow and heat transfer in two adjacent flow channels (water/water and water/oil respectively) of a chevron sinusoidal corrugated plate. The distributions of the overall temperature, heat flux density, and mass flow rate in the channel were obtained. The results showed that, under the calculation conditions, the fluid in the hot channel flew in a *Z*-shape along the mainstream direction. Liu et al. [18] used Fluent software to carry out numerical simulation research on single-phase water flow in chevron flow channel, who's *Re* was set from 660 to 2200. The flow distribution near the contact point and fully developed area had been considered and the variation law of velocity and pressure at each special section had been summarized. When the chevron angle was 60°, a parallel *Z*-shaped flow was formed along the mainstream direction; The high shear force on the wall near the center point of the corrugated plate easily led to the deviation of the mainstream direction of the fluid. Roetzel et al. [19] used temperature oscillation technology to carry out experimental evaluation on the thermal properties of PHE, and used mathematical models to calculate the heat transfer coefficient characterized by the number of heat transfer units and Peklet number.

Owing to the coupling effect between various parameters, professional optimization algorithms were adopted to explore the optimal solution in recent years. Hamed [20] utilized the NSGA-II algorithm to achieve multi-objective optimization in spiral corrugated pipes and obtained the optimal solutions. Optimized correlations could also be used for the thermal design of fluid flow in spiral corrugated pipes. A novel hybrid optimization approach was proposed by Hossein [21] and the particle swarm optimization method was used by Ocłoń [22], an improved design was proposed. In order to improve the shape of fins in aerospace applications, Bashir [23] developed a new algorithm based on genetic algorithm (GA) combined with CFD.

From the above literatures, it could be concluded that the research on parameterization of chevron corrugated plates had been quite complete, while the further research on chevron sinusoidal corrugated plates was needed; Besides, the structural optimization of plate heat exchangers had gradually developed from single objective optimization to multi-objective optimization. Therefore, this article had decided to take a single flow channel in a chevron sinusoidal corrugated plate heat exchanger as the object of research, and used a combination of CFD numerical simulation and machine learning method to explore the influence of the angle, height, and pitch of the chevron sinusoidal corrugation, and ultimately obtain the optimal parameters after optimization.

2. Numerical methodology

2.1. Geometry of the model

For the numerical study of welded plate heat exchangers, this paper conducted a model of the single flow channel between two chevron sinusoidal corrugated plates, which included the inlet section, outlet section and test section. Fig. 1 showed a three-dimensional model of the welded plate heat exchanger proposed in this study. Among them, the length of the test section was 180 mm, and the arrangements of the inlet and outlet sections were mainly to ensure the complete development of

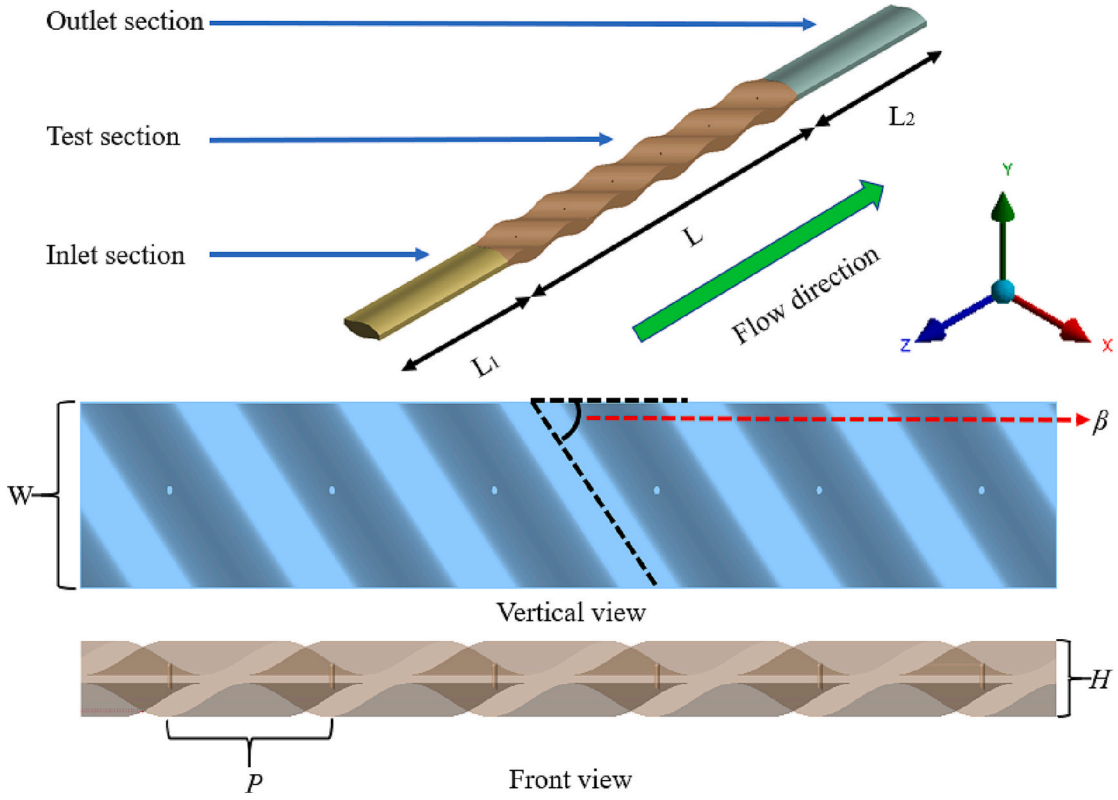

Fig. 1. 3D schematic diagram of the flow channel.

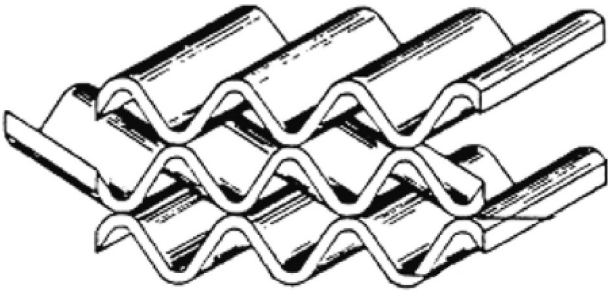

Fig. 2. The structural schematic diagram of the plates.

Table 1
Specific parameters of the model

Parameters of the plate	unit	value
Length of the test section(L)	mm	180
Width of the test section(W)	mm	22
Length of the inlet section(L_1)	mm	80
Length of the outlet section(L_2)	mm	80
Total height of corrugation (H)	mm	3, 5, 7, 9
Pitch of corrugation (P)	mm	15, 20, 30, 45, 60
Chevron angle(β)	degree	30,45,60

the working fluid flow and prevent backflow at the outlet of the test section. The length of both two sections were 80 mm. The flow channel of the plate exchange was formed by squeezing two parallel corrugated plates with opposite directions, so there were several contact points inside the flow channel, the structural schematic diagram was shown in Fig. 2. To facilitate subsequent calculations, this study cut out a circular hole with a diameter of 1 mm in the intersection of the corrugations as the contact point between the two plates. The specific geometric parameters of the flow channel were shown in Table 1.

2.2. Mathematical modeling

Before conducting numerical simulation, some basic assumptions needed to be proposed:(1) The selected working fluid was an incompressible, continuous and Newtonian fluid;(2) This study did not take phase transition of the working fluid into account; (3) Thermal radiation and buoyancy force were also not considered; Based on the above assumptions, the numerical formula for this study were as follows:

The continuity equation, also known as the conservation of mass equation, was expressed as:

$$\frac{\partial u_i}{\partial x_i} = 0 (i = 1 \sim 3) \tag{1}$$

Momentum equation:

$$\rho u_i \frac{\partial u_j}{\partial x_i} = -\frac{\partial p}{\partial x_i} + \frac{\partial}{\partial x_i}\left(\mu \frac{\partial u_j}{\partial x_i}\right) (i,j = 1 \sim 3) \tag{2}$$

The energy equation was essentially the first law of thermodynamics, which must be followed for heat exchange during fluid flow. Its expression was as follows:

$$\rho c_p \left(u_i \frac{\partial T}{\partial x_i}\right) = \lambda \left(\frac{\partial^2 T}{\partial x_i^2}\right) (i = 1 \sim 3) \tag{3}$$

Turbulent flow was a common form of flow in daily life, which was not a regular and slow flow like laminar flow. Instead, it was a chaotic flow composed of vortices of different sizes. These vortices had nonlinear random motion in time and space when they flowing in the mainstream direction. Therefore, turbulence was an irregular flow that was often used to enhance heat transfer. When solving problems involving turbulent flow, it was necessary to comprehensively consider the performance of the computing equipment and the flow form of the research object in order to quickly and accurately obtain the corresponding results. Therefore, suitable turbulence models should be selected for simulations in different turbulence problems. At present, the

standard k-ε model, Realizable k-ε model, and RNG k-ε model were most widely used in engineering [24]. Some scholars have evaluated and compared the three turbulence models and ultimately found that the RNG k-ε model could handle flows with high streamline curvature and high strain rates [25]. Therefore, the RNG k-ε model was used in this design.

Based on the theory of the standard model, RNG added an item to the equation of ε, corrected the dissipation rate equation, improved the calculation accuracy, changed the calculation formula of turbulent viscosity, considered the influence of complex eddy currents on turbulence, derived the relevant formula of flow viscosity under the condition of low Reynolds number, showing a small-scale effect on large-scale flow and the corrected viscosity item. Compared with the standard k - ε model, it was suitable for the fully developed high *Re* turbulence model, and has a higher reliability for the calculation of more complex fluid problems such as shear flow, flow separation and secondary flow. Its expression was as follows:

$$\frac{\partial}{\partial t}(\rho k)+\frac{\partial}{\partial x_i}(\rho k u_i)=\frac{\partial}{\partial x_j}\left(a_k \mu_{eff}\frac{\partial k}{\partial x_j}\right)+G_k-\rho\varepsilon \tag{4}$$

$$\frac{\partial}{\partial t}(\rho \varepsilon)+\frac{\partial}{\partial x_i}(\rho \varepsilon u_i)=\frac{\partial}{\partial x_j}\left(a_\varepsilon \mu_{eff}\frac{\partial \varepsilon}{\partial x_j}\right)+C_{1\varepsilon}G_k\frac{\varepsilon}{k}-C_{2\varepsilon}\rho\frac{\varepsilon^2}{k} \tag{5}$$

where G_k represented the turbulent kinetic energy.

2.3. Boundary conditions

The inlet boundary condition selected the velocity inlet, and the temperature of the working fluid was constant at 363.15 K. The velocity of inlet flow was set from 0.1 m/s to 0. 5 m/s while the corresponding range of *Re* was from 1821 to 9106. Meanwhile, the outlet section was set as a pressure outlet. The left and right walls of the test section were both set as adiabatic boundaries rather than symmetry boundaries due to their different shapes; Besides, the upper and down walls were set as a constant temperature, with a constant wall temperature of 288.15 K. All other interfaces were set as the type of interior and the details of the boundary conditions were also shown in Fig. 3. The settings of the above boundary conditions were all based on the relevant work of previous scholars in the research of plate heat exchangers [26]. In the simulation solution method, the momentum and energy equations in the spatial discrete part were selected as second-order upwind, and the gradient solution was selected as Least squares cell based. The residuals of the continuity, momentum and energy equations were set as 10^{-6}. All simulation work in this article was achieved through fluent 19.0.

In addition, aluminum was selected as the main material for each component, and water was used as the working fluid at the hot end. The specific parameters of the working fluid were shown in Table 2 [27].

Table 2
Thermo-physical properties of water

Thermo-physical properties	Value
ρ	998.2 kg/m^3
λ	0.6 W/(m·K)
μ	1.003 × 10^{-3} kg/(m·s)
c	4182 J/(kg·K)

2.4. Data reduction

Nu, *f* and *Re* [28], as the main measuring indicators, could be expressed as:

$$\mathrm{Nu}=\frac{\mathrm{Dh}}{\lambda} \tag{6}$$

$$\mathrm{f}=\frac{2\mathrm{D}\Delta\mathrm{P}}{L\rho\mathrm{u}^2} \tag{7}$$

$$Re=\frac{\rho \mathrm{Du}}{\mu} \tag{8}$$

Except that, other main indicators were also given as follow:

$$\mathrm{h}=\frac{\mathrm{Q}}{\mathrm{A_{ht}}\Delta\mathrm{t_m}} \tag{9}$$

$$\mathrm{Q}=\mathrm{cg}|\mathrm{t_{in}}-\mathrm{t_{out}}| \tag{10}$$

$$\Delta\mathrm{t_m}=\frac{\mathrm{t_{max}}-\mathrm{t_{min}}}{ln\frac{\mathrm{t_{max}}}{\mathrm{t_{min}}}} \tag{11}$$

where *c*, *g* and A_{ht} represented specific heat capacity of the working fluid, mass flow rate in flow channel and the area of heated wall, respectively.

In order to verify the optimization effect of the designed structure, *JF* [29] was selected as the evaluation index for evaluating the comprehensive performance of WPHE, its expression was given as:

$$j=\frac{Nu}{Re}\cdot Pr^{-\frac{1}{3}} \tag{12}$$

$$JF=\frac{j}{f^{\frac{1}{3}}} \tag{13}$$

2.5. Meshing independence

In the process of numerical simulation calculation, the meshing of the computational domain was the most important step, which directly affected the accuracy of the simulation results. High quality grids not only ensured the accuracy of the calculation results, but also improved the speed of calculation convergence. For the existing geometric modeling, the test section was the main research area, and this study

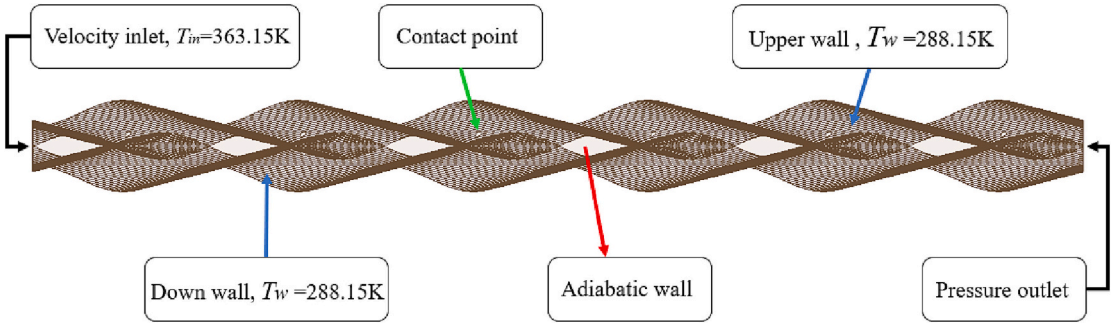

Fig. 3. Specific settings of boundary conditions.

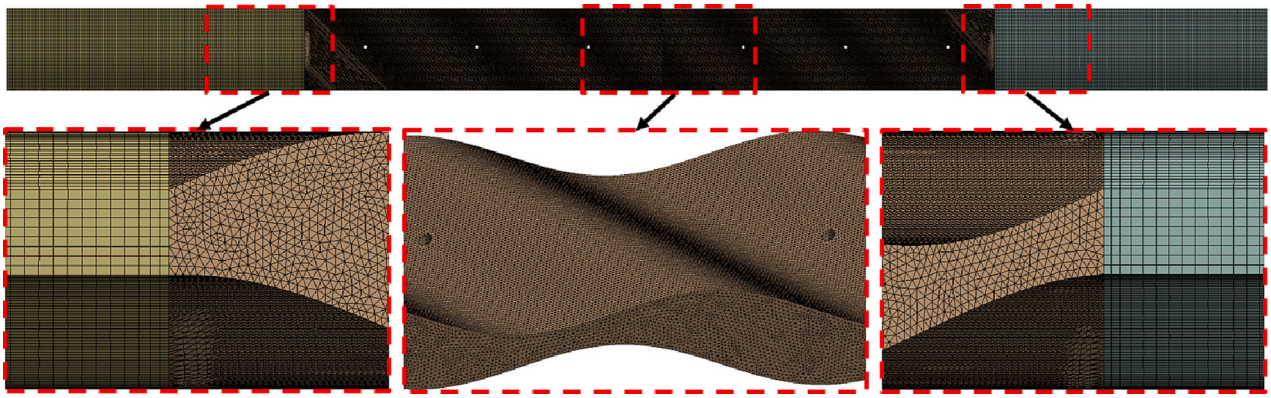

Fig. 4. Grids for numerical simulations.

Table 3
Grid independence test

Total element number	*Nu*	*f*
1,065,419	246.135	0.7921
3,203,125	250.943	0.8101
6,690,759	258.551	0.8916
8,735,446	258.966	0.8986
11,416,892	259.129	0.903

chose unstructured tetrahedral grid generation for it, with the grid size set as 0.3 mm; The inlet and outlet sections, on the other hand, adopt a sweeping division method to save time and computational resources. The grid size was set as 0.5 mm. The specific grid division was shown in the Fig. 4.

In order to better capture the temperature and velocity boundary layer, this article also made appropriate settings for non-dimensional y + parameter. Finally, the value of y + was set in the range of 0.58– 0.86 when *Re* was from 1821 to 9106. According to the Fluent users' guide [28], the boundary layers could be well captured if the y + less than 1. Thus, this grid division method was suitable for subsequent research.

The number of grids is often determined by the partitioning method and grid size. The smaller the grid, the corresponding increase in the number of grids, the higher the requirements for computer performance, and the longer the time spent. However, the calculation results did not always change with the number of grids. When the number of grids increased to a certain value, the calculation results tended to stabilize. Therefore, finding out the appropriate number of grids was particularly important in the numerical simulation process, as it could not only improve computational accuracy but also saved time and cost. Therefore, it was necessary to carry out relevant work on grid independence verification. This study provided a total of five different numbers of grids at a flow rate of 0.1 m/s. It was not difficult to observe from the Table 3 that when the number of grids reached 6.69 million, the relative errors of *Nu* and *f* in the flow channel were already small enough. Therefore, 6.69 million grids were ultimately selected as the number of grids for this study.

2.6. Model validation

In order to verify the authenticity and reliability of the model and simulation results in this article, the simulation results were compared with Focke's experimental data [29]. Fig. 5 showed the distribution of *f* between the two. The conclusion drawn from the figure was that under the same *Re*, the maximum relative error of the two was 14.11%, while the minimum error was only 4.52%, and the calculated average error

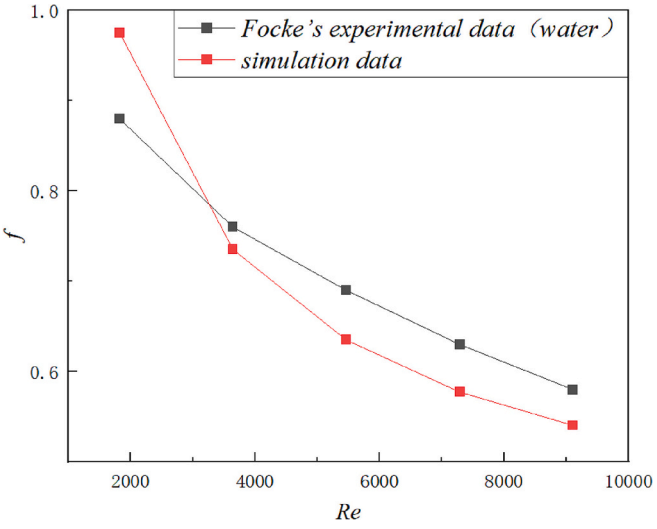

Fig. 5. Verification between simulation data and experimental data.

was 9%. Good fitting also provided assurance for the accuracy of subsequent simulations.

3. Optimization method

3.1. The principles and processes of optimization

Due to the strong coupling effect between various parameters, the optimal parameters obtained from parameter analysis cannot represent the optimal structure. In this case, optimization algorithms needed to be used to solve for the optimal results. It should be noted that multi-objective optimization algorithms optimize multiple mutually exclusive objective functions simultaneously, resulting in a set of non-inferior solutions rather than a specific solution. As a commonly used optimization algorithm, multi-objective genetic algorithm (MOGA) [30] was selected to provide Pareto solutions in this paper.

Before algorithm optimization, a suitable surrogate model was needed. This article used artificial neural networks (ANNs) to express the relationship between geometric parameters and optimization objectives. First, multiple groups of data calculated by numerical simulation were imported into ANN for training, and a surrogate model containing the relationship between geometric parameters and optimization objectives could be obtained. Then, the surrogate model was

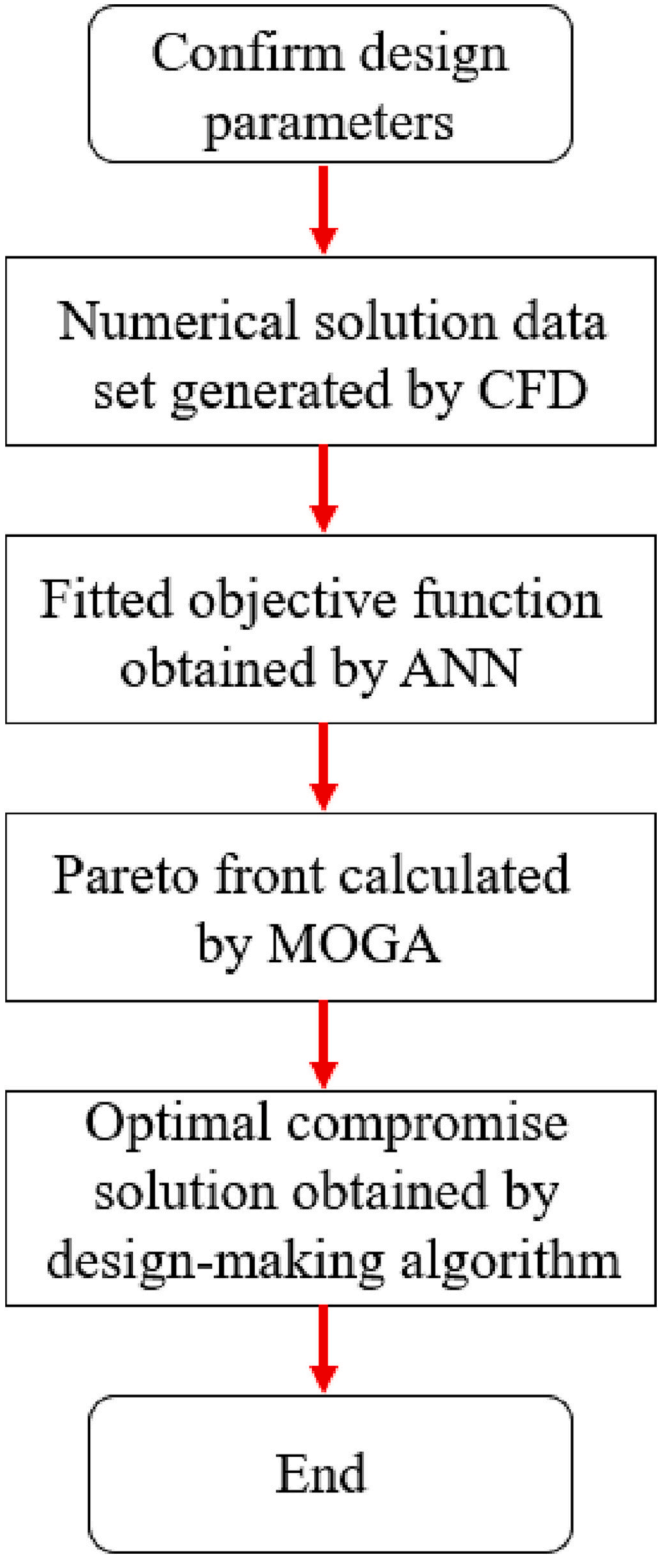

Fig. 6. The optimization program.

optimized by optimization algorithm and pareto front was obtained. The optimization process was shown in Fig. 6.

3.2. Design of ANNs

Optimizing the structure of the flow channel not only increased the heat transfer area and changed the form of flow, but also accompanied an increase in Δp, resulting in an increase in flow resistance. Therefore, in this study, the two mutually constrained indicators, Nu and ΔP, were selected as optimization objectives, and their definitions were as follow:

$$J_1 = Nu \tag{14}$$

$$J_2 = \Delta p \tag{15}$$

The network consisted of three layers: input layer, hidden layer, and output layer. In this study, the proportion of data in the training, validation, and testing sets was set to 70%, 15%, and 15%, respectively. Eq. (18) represented the correlation between normalized J_1 and J_2.

$$J_1 \text{ or } J_2 = \sum_{j=1}^{m} w_{1j} \left(\frac{2}{1 + e^{-2\left(\sum_{i=1}^{3} w_{ji} x_i + b_j\right)}} - 1 \right) + b_k \tag{16}$$

The mean square error (MSE) and regression coefficient (R^2) could effectively evaluate fitting performance of neural networks. The larger R^2, the smaller MSE, and the higher the accuracy of ANNs; Their mathematical expressions were as follows:

$$MSE = \frac{1}{N}\sum_{i=1}^{n} \left(y_{i,ANN} - y_i\right)^2 \tag{17}$$

$$R^2 = 1 - \sum_{i=1}^{N} \frac{\left(y_{i,ANN} - y_i\right)^2}{y_i^2} \tag{18}$$

4. Result and discussion

4.1. Analyses on flow field

The distribution of streamlines in the flow channel of a welded plate heat exchanger had been shown in Fig. 7. From the picture, it could be analyzed that the flow velocity of the outer fluid which near the wall and local area near the contact point were relatively low. The main reason was that the outer fluid was easily squeezed by the inner fluid and generated a tangential force perpendicular to the direction of the flow channel. Therefore, the flow form of the outer fluid generally turned to cross flow, the flow rate decreased sharply and secondary flow was also formed easily. In addition, Fig. 7(a), (b) and (c) had displayed the distribution of the streamlines in front of the contact area, around the contact area and behind the contact area, respectively. The above three local images of different cross-sections in the flow channel could also confirm this opinion. On the other hand, the inner fluid far from the contact point was slightly disturbed, and the flow pattern was similar to that of the flat plate. The velocity distribution of the flat plate was provided in Fig. 8. The inner fluid near the contact point was disturbed the contact part, thus the average velocity of this part was lower than that of the others.

Fig. 9 mainly showed the temperature, velocity, and pressure distribution of a certain cross-section when the velocity was set as 0.3 m/s. It was obvious to find that the space of the connecting line area between the contact points in the flow channel was relatively narrow, so the average velocity of that area was relatively slow. Due to the decrease in turbulence intensity, the tangential force perpendicular to the flow direction was also significantly reduced, causing the fluid passing through the contact point to spray out at high speed along the direction of the flow channel, while the average flow velocity in the local area behind the contact point was relatively low. However, the heat transfer area in the narrow channel has also been increased, and a large number of working fluids converged here from all directions, and the mixing of the working fluid was quite sufficient, so the heat transfer could be enhanced in this area. This point could also be verified in the

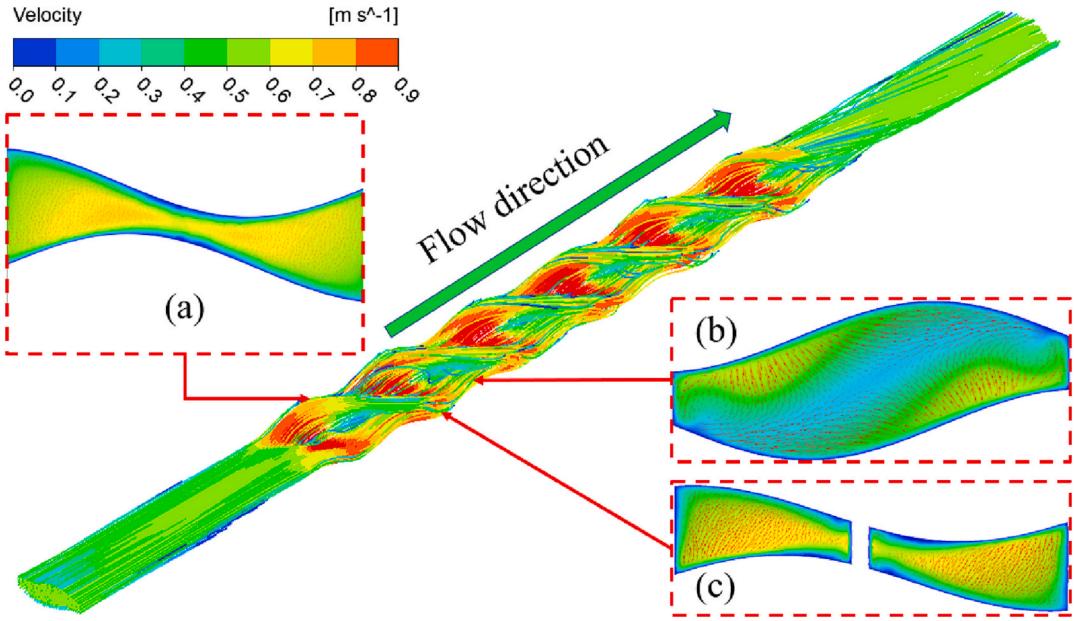

Fig. 7. The streamlines distribution of the flow channel.

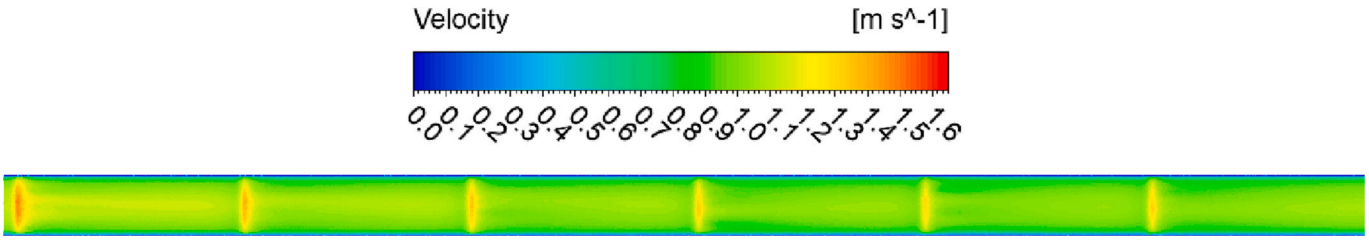

Fig. 8. Velocity distribution of the flat plate.

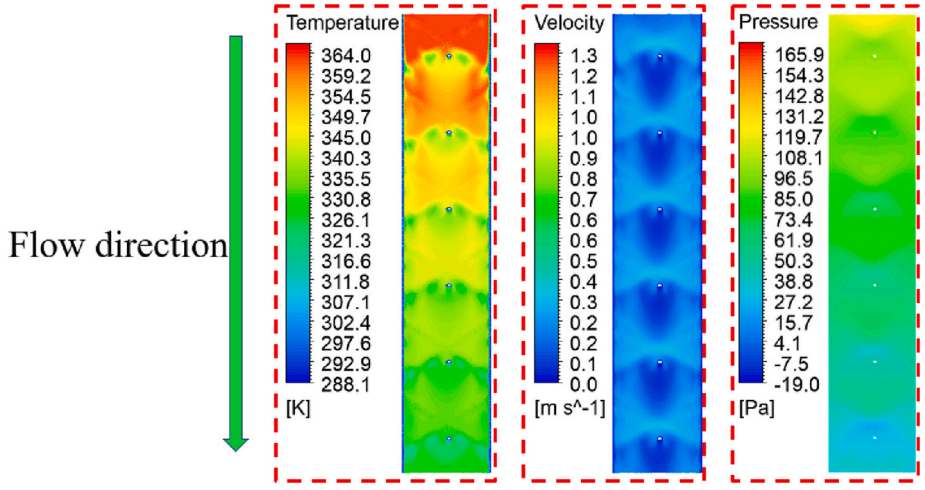

Fig. 9. The Temperature, Velocity and Pressure distributions of a selected cross section.

temperature distribution of the cross section, and the average temperature of working fluids decreased significantly after flowing through the narrow area; The distribution of the pressure once again indicated that the corrugated structure of the plate will accelerate the decrease of pressure in the flow channel, and compared with flat plate, the Δp increased by 2.79– 6.37 times.

4.2. *The effect of H in flow channels*

Fig. 10 showed the distributions of temperature in a longitudinal section under different H, it could be observed that as the height of the corrugations increased, the average temperature at the same position in the flow channel decreased sharply, and the difference of temperature between the inlet and outlet of the flow channel gradually increased. These effects indicated that with the increase of H, the heat transfer

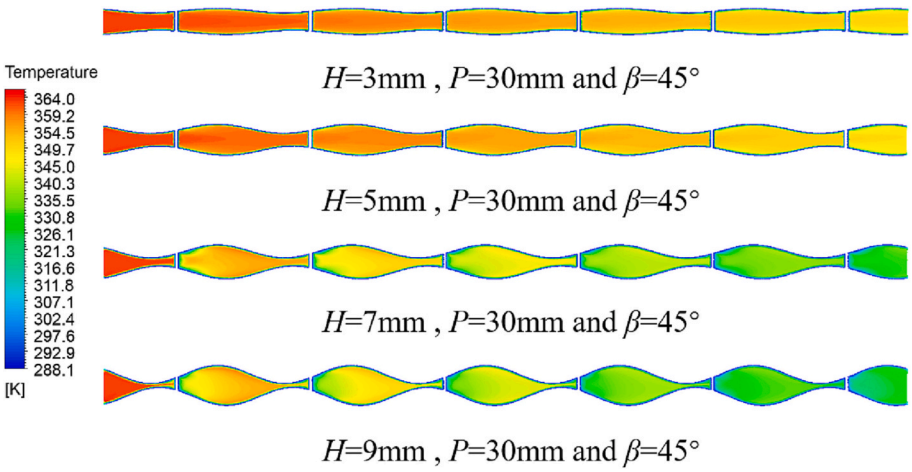

Fig. 10. The distributions of temperature in a longitudinal section under different *H*.

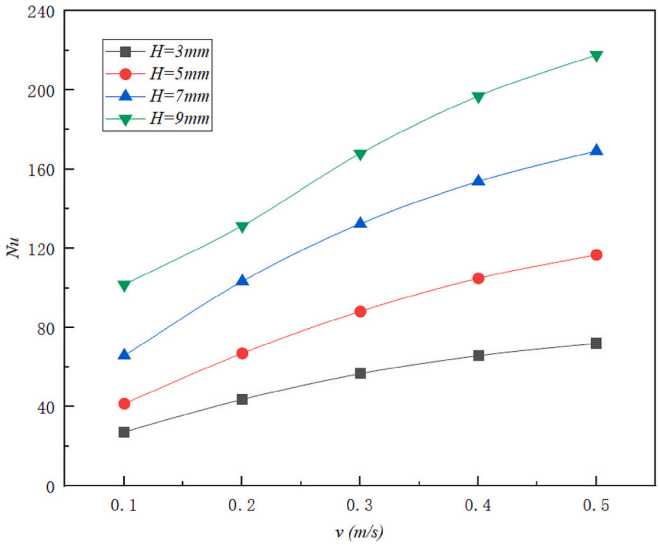

Fig. 11. The effect of *H* on *Nu* under different velocities.

efficiency in the flow channel was improved. The main reason might be the total heat transfer area obviously increased, and fluid mixing in the flow channel became more and more uniform and sufficient. In addition, within the same period, the average temperature of the area near contact point was lower than that of others, which also confirmed the changing in the flow form of the working fluid, exacerbating the mixing between fluids and promoting the heat transfer efficiency of this area.

The effect of height on *Nu* under different velocities was displayed in Fig. 11. As the speed increased, the turbulence intensity increased instead, and the heat transfer capacity in the flow channel was also enhanced; Furthermore, the increase in velocity would enlarge the deviation of *Nu* between structures under different *H*. According to the results, *Nu* increased by 3.02–3.71 times when the height increased from 3 mm to 9 mm.

The distribution of velocity in longitudinal section could represent the flow characteristics in the channel more intuitively. As shown in Fig. 12, with the space inside the channel continuously compressed, a large number of working fluids refracted from different channels gather at the front of the contact point, resulting in a higher average velocity in this area. As the height decreased, the velocity of the working fluid gradually became uniform within the same cycle. The inner fluid had a relatively small disturbance and a higher velocity, while the flow rate in the local area behind the contact point was relatively low. However, as it developed, the flow rate will continue to increased and eventually converged with the fluid from other areas at the front of the next contact point.

The structure of corrugated plate would inevitably increase the resistance and pressure drop in the flow channel, which could also be seen from Fig. 13. In addition, as the velocity of the fluid increased, the variation amplitude of the resistance coefficient would become smaller

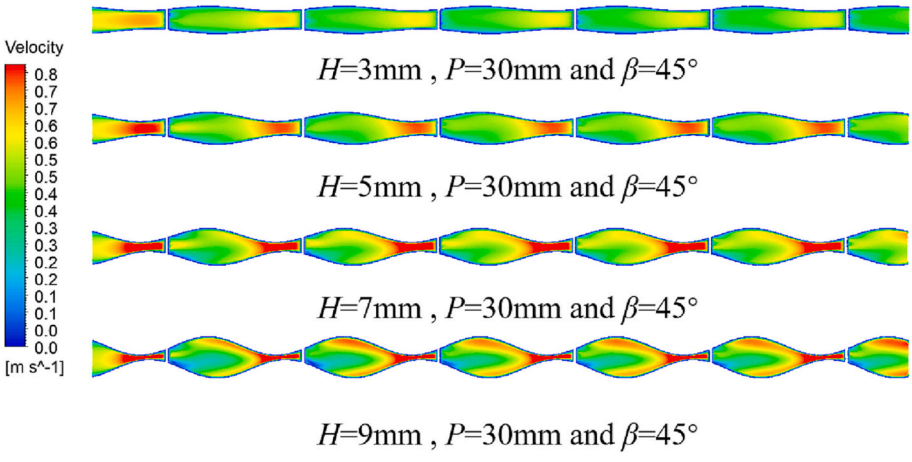

Fig. 12. The distributions of velocity in a longitudinal section under different *H*.

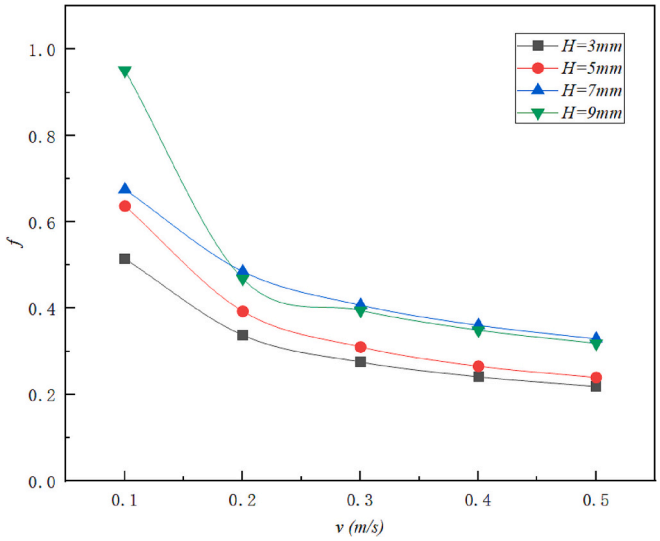

Fig. 13. The effect of H on f under different velocities.

and smaller. The peak of the f occurred at the speed of 0.1 m/s, and the increase factor reached 1.91.

4.3. The effect of β in flow channels

Fig. 14 represented the distributions of temperature in a cross section under different β. The increase in β was accompanied by a decrease in the number of corrugations in the flow channel, resulting in a decrease in the total heat transfer area and heat transfer efficiency. The Nu naturally decreased with the increase of β, which could also be verified in Fig. 15. Therefore, within the range considered in this article, the thermal performance of $\beta = 30°$was the best, with the maximum temperature difference between the inlet and outlet. In addition, it could be seen from the Fig. 15 that as the velocity increased, the improvement of heat transfer performance became gentle.

Fig. 16 represented the distributions of velocity in a cross section under different β. As mentioned above, the total heat transfer area in the flow channel gradually increased with the decrease of β, and it would also be accompanied by an increase in along resistance. Therefore, the f at 30° was significantly higher than that of the other two structures. It could be verified from Fig. 17. Besides, it could also be concluded from Fig. 16 that the area of the low-speed area behind the contact point would increase as the β increased. Attributed to low resistance, high flow rates might prone to create dead zones.

4.4. The effect of P in flow channels

The distributions of temperature in a cross section under different P had been shown in Fig. 18. The decrease of P gradually increased the number of corrugations, making the structure more complex, and the total heat transfer area in the flow channel also gradually increased accordingly. Therefore, it was not difficult to observe that as P decreased, the thermal performance continuously enhanced; When P was set as 15 mm, the thermal performance in the flow channel was the best, and the difference of temperature between the inlet and outlet was also the largest.

Fig. 19 showed the effect of P on Nu under different velocities. The content in the figure confirmed the above opinion. In addition, it could also be concluded that as the speed increased, the heat transfer performance gradually deteriorated. The main reason might be that the excessively high velocity created dead zones of heat transfer in the flow channel, which were not conducive to the enhancement of heat transfer.

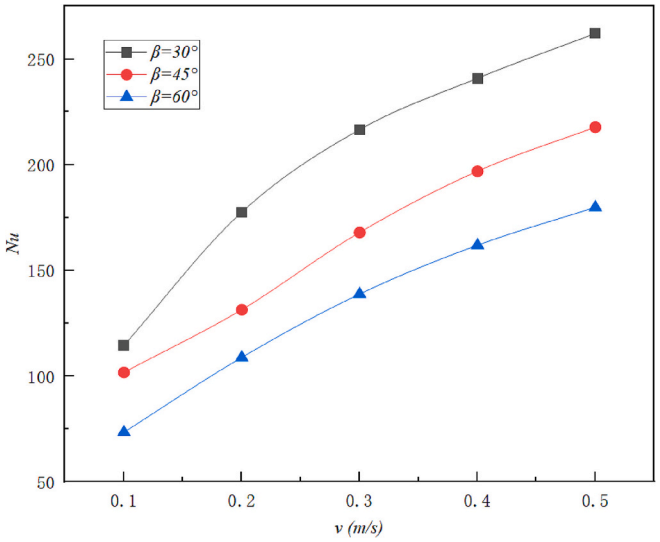

Fig. 15. The effect of β on Nu under different velocities.

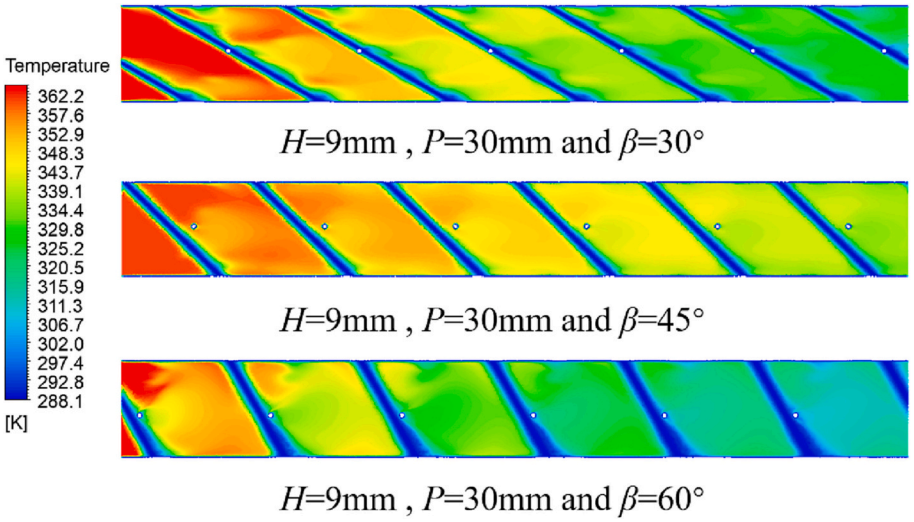

Fig. 14. The distributions of temperature in a cross section under different β.

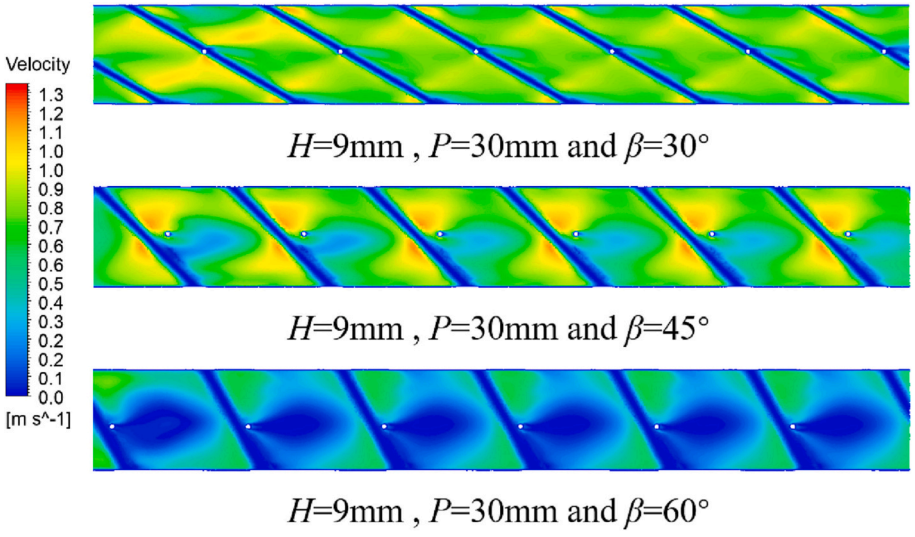

Fig. 16. The distributions of velocity in a cross section under different β.

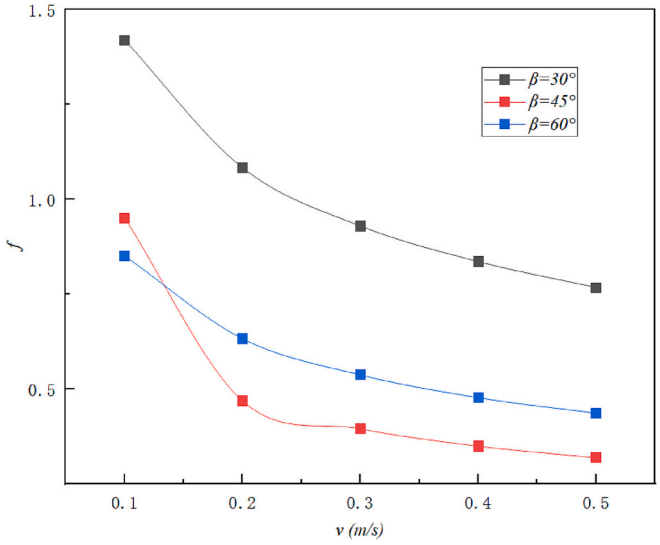

Fig. 17. The effect of β on f under different velocities.

The distributions of velocity in a cross section under different P was displayed in Fig. 20. The average velocity in the area near the contact point was obviously higher than that in other areas, and the flow pattern in the flow channel was described earlier. The complexity of the flow channel led to continuous changes in the flow form, and the average velocity also significantly increased.

Fig. 21 represented the effect of P on f under different velocities. It could be observed that when PP was set as 15 mm and 20 mm, the flow resistance in the channel was significantly higher than that of other structures. Compared to the case of $P = 60$ mm, f could be increased by up to 4.53 times as the P set as 15 mm. As the flow rate increased, the trend of resistance changing became gentle.

4.5. Comprehensive evaluation based on parameter analysis

The variation of *JF* of WPHE with flow velocity under three geometric variables had been shown in Fig. 22. Generally, the higher the corrugations height, the better the overall performance of the corrugated plate. However, the *JF* of the corrugated plate with a height of 5 mm was slightly lower than that with a height of 3 mm when the flow rate reached 0.4 m/s. This phenomenon indicated that the influence of resistance in the flow channel was stronger than the strengthening effect of heat transfer; Within the range of this paper, the *JF* factor reached the highest when the height was designed as 9 mm, reaching 0.043; In terms of angle β, the comprehensive performance of the two types of plates with angles of 30°and 60° was relatively close, while the comprehensive performance of the plate with angle of 45° was significantly stronger than the other two. When the flow rate reached 0.3 m/s, *JF* reached a peak of 0.042; Pitch was the most important factor affecting the structure of the plate. When the pitch was the smallest, the number of corrugated plates was the highest. When the pitch was taken as 30 mm, the plate could have a better comprehensive performance, and it also reached its peak at a flow rate of 0.3 m/s.

5. Results of optimization

5.1. Analysis of ANNs

In the previous parameter analysis, it was observed that chevron angle β, height H, and pitch P had a significant impact on the thermo-hydraulic performance in the flow channel. Hence , the above three design variables were used as optimization solutions, as shown in the Tables 1,3,4 and 5 levels were chosen for β, H and P, respectively. A total of 60 numerical data would be imported into ANNs for training.

The number of hidden layer neurons directly determined the accuracy of ANNs fitting function. Fewer neurons might cause insufficient training effect of simulation data and failure to capture data characteristics, while too more neurons might lead to overfitting. In order to avoid both of the above situations, this section tested the number of hidden layer neurons, and the fitting effects under different numbers of hidden layer neurons were shown in the Table 4. The final results showed that the optimal number of hidden layer neurons for two objective functions both were 7.

In addition, the CFD data was compared and validated with the model data trained by ANNs, and the final results from Fig. 23 showed a good match between the two, with maximum errors of 13.7% and 8.4%, respectively.

5.2. Multi-objective optimization results analysis

Minimization: $J_1 = f_1(\beta, H, W)$ and $J_2 = f_2(\beta, H, W)$.
Subject to: $\beta \in [30,60]$, $H \in [3,9]$ and $W \in [15,60]$.
This article prepared to use MOGA to optimize the two conflicting

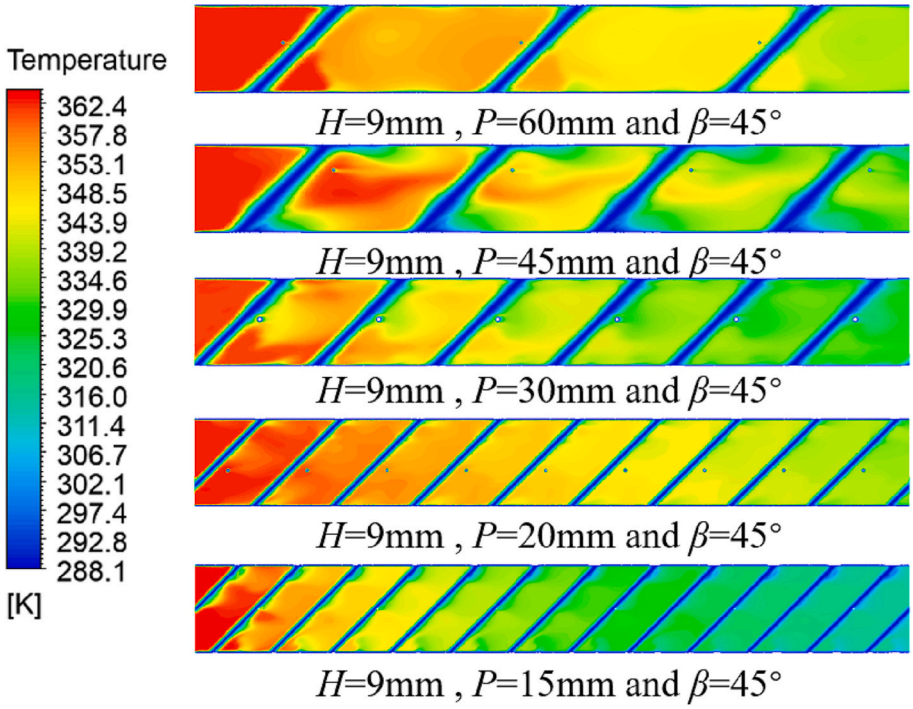

Fig. 18. The distributions of temperature in a cross section under different *P*.

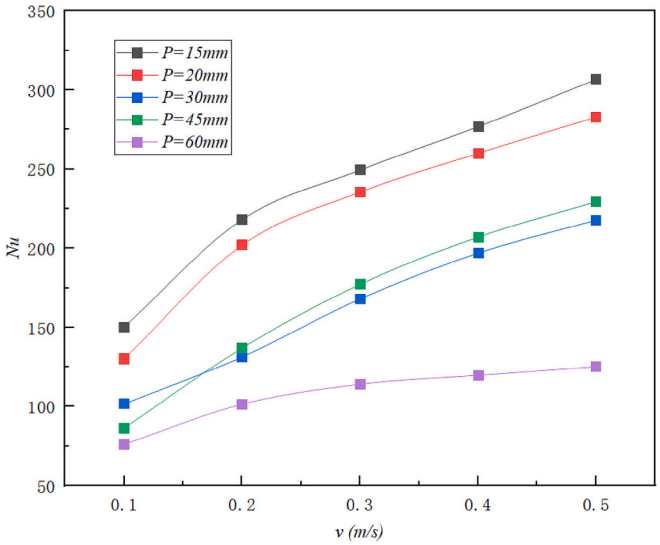

Fig. 19. The effect of *P* on *Nu* under different velocities.

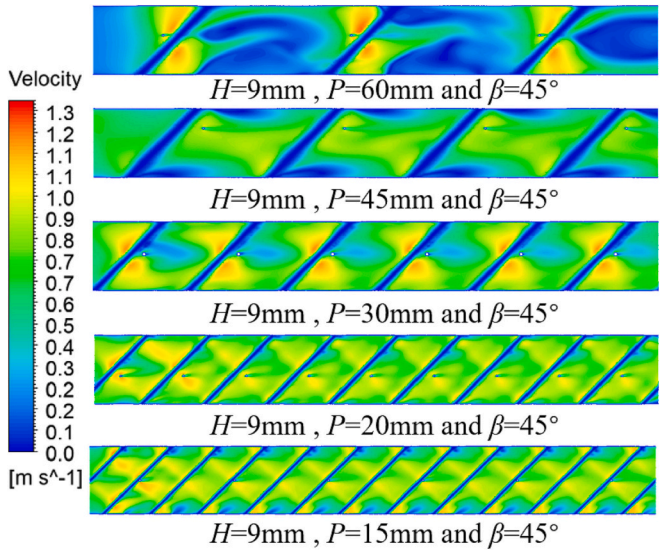

Fig. 20. The distributions of velocity in a cross section under different P.

objectives as mentioned above. In addition, the relevant working conditions of the algorithm could be found in Table 5. What's more, all points located at the front of Pareto were globally optimal. Moving along the Pareto frontier, when one optimization goal improved, the other one would inevitably deteriorated. From the results, it could be seen from Fig. 23 that the range of the Pareto front obtained by MOGA was considerable and suitable for this study. The optimal ranging of *Nu* was from 29.83 to 96.42 and the optimal ranging of ΔP was from 131.28 Pa to 331.26 Pa.

5.3. Optimal compromise solution selection and comparison

How to obtain the optimal compromise solution from several non-inferior solutions was the key to this article. The main principle of the classic decision algorithm TOPSIS had been introduced in relevant literature [31] in detail.

According to reference [31], two optimization objectives had equal importance. In order to obtain the optimal compromise solution that met practical requirements, this parameter could be adjusted accordingly in different situations.

Fig. 24 showed the distribution of closeness between each non-inferior solution and the ideal optimal solution. The ranking scores of both endpoints A and B were relatively low, indicating that improving a single objective function would lead to a decrease in overall performance. Therefore, this article ultimately chose point C, which was close to the maximum value. The results showed that the value of JF at point C

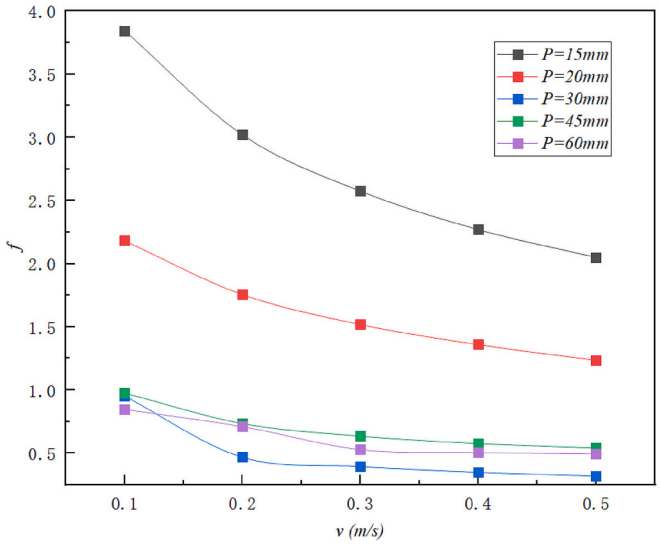

Fig. 21. The effect of P on f under different velocities.

Table 4
Neuron independence verification for J_1 and J_2.

Number of neurons	$J_1 = Nu$		$J_2 = \Delta P$	
	MSE	R^2	MSE	R^2
1	0.00825	0.840	0.0118	0.688
2	0.00484	0.906	0.0063	0.792
3	0.00579	0.904	0.0032	0.913
4	0.00334	0.943	0.0012	0.958
5	0.00453	0.931	0.0013	0.973
6	0.00384	0.939	0.0011	0.973
7	0.00190	0.964	0.0004	0.987
8	0.00447	0.923	0.0007	0.984
9	0.00410	0.928	0.0020	0.949
10	0.00577	0.894	0.0005	0.984
11	0.00239	0.927	0.0010	0.981
12	0.00342	0.927	0.0012	0.963
13	0.00865	0.746	0.0012	0.963
14	0.00599	0.881	0.0018	0.891
15	0.00353	0.898	0.0015	0.958

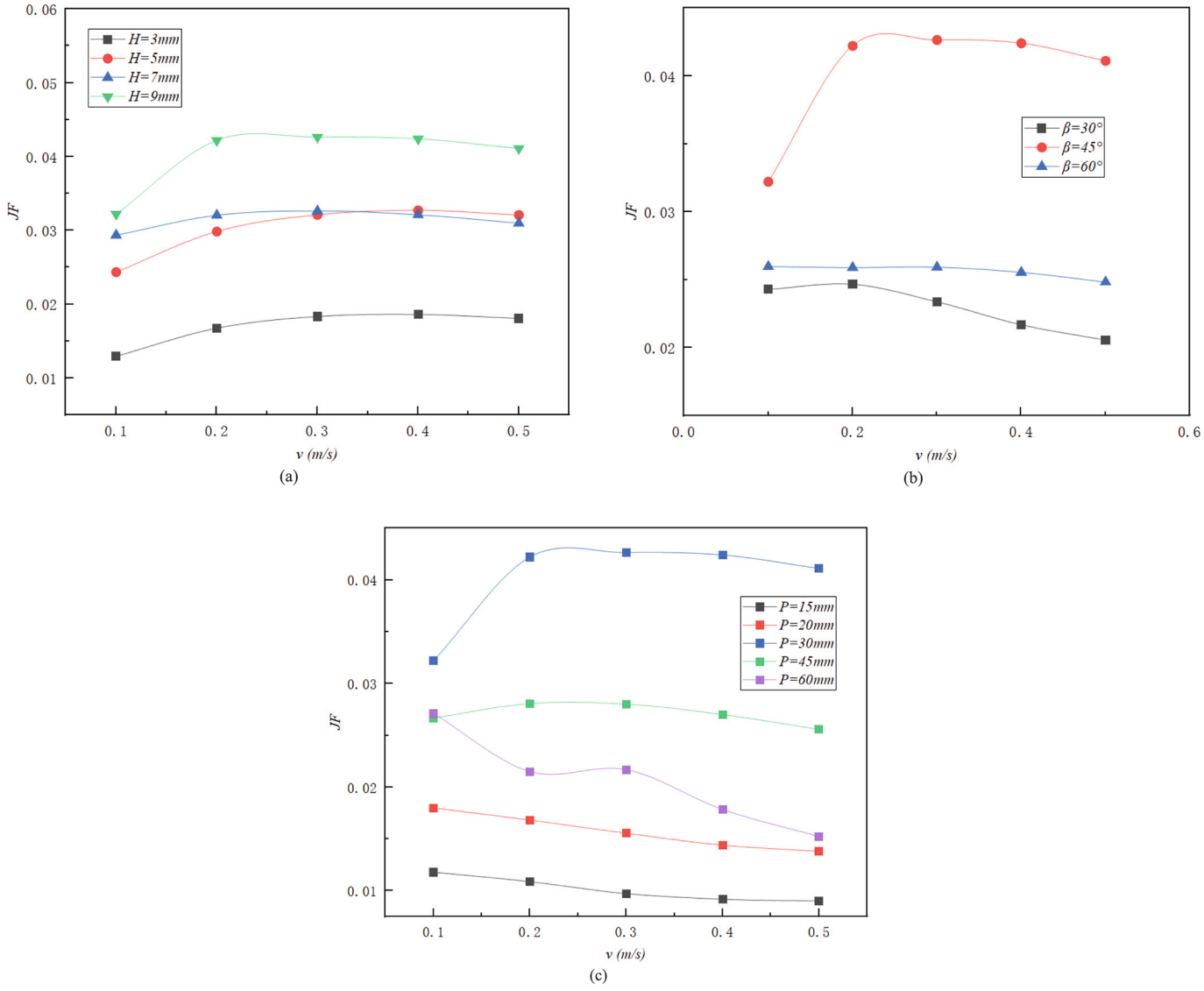

Fig. 22. The JF of three variables under different velocities: (a) H; (b) β; (c) P.

Table 5
Multi-objective optimization results analysis

MOGA	Population size	500
	Pareto fraction	0.2
	Generation	100
	Migration fraction	0.2
	Crossover fraction	0.8
	Function tolerance	5×10^{-5}

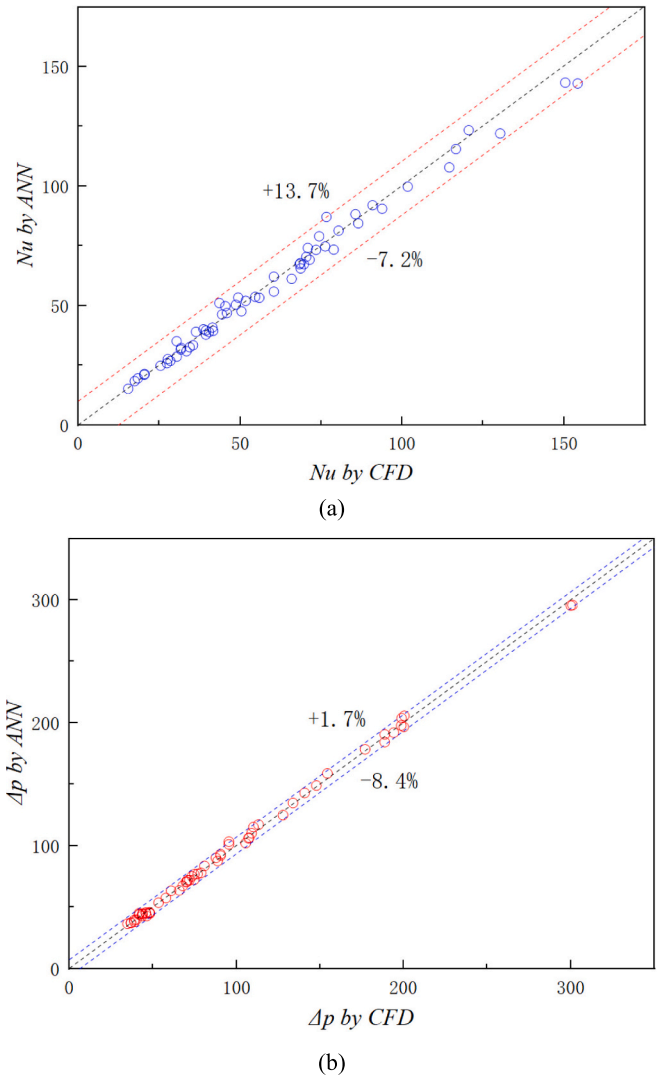

Fig. 23. Comparison of CFD values with ANN predicted values: (a) *Nu*; (b) *ΔP*.

was slightly higher than that of points A and B, reaching 0.034. Under the same working conditions, the optimized structure had the best thermal-hydraulic performance.

At the end of this article, point A, B, and C were re-modeled and re-calculated. Table 6 showed the structural parameters corresponding to points A, B, and C and the relevant results were shown in Table 7. Under the same working conditions, the simulation results obtained were generally consistent with the predicted values of the ANNs, with a relative error of less than 4%. This further confirmed the accuracy of the prediction model proposed in this paper.

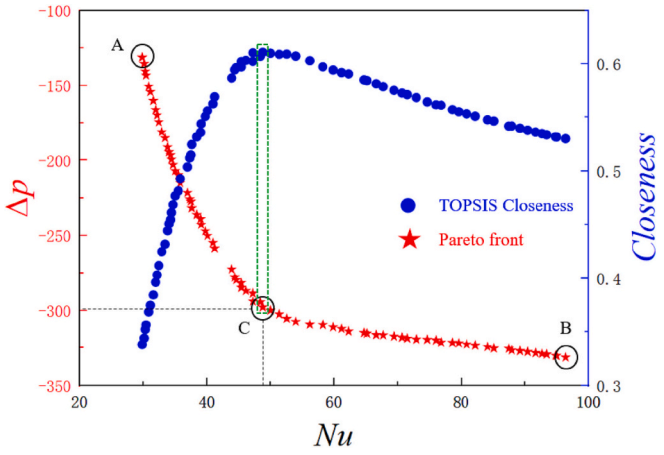

Fig. 24. The Pareto front of MOGA and variation in relative closeness.

Table 6
Geometrical parameters of different solutions

Solutions	Geometrical parameters		
	H, mm	*β*	*P*, mm
A, *Nu* minimization	3.003	44.772	25.141
B,Δ*p* minimization	3.002	52.193	15.008
C, TOPSIS	3.005	45.495	15.132

Table 7
Verification of the solutions on the Pareto front

Solution	Objectives	Predicted value by ANN	Calculated value by CFD	Relative error
A, *Nu* minimization	*Nu*	29.83	28.88	3.29%
	Δ*p*	131.28	133.04	1.32%
B,Δ*p* minimization	*Nu*	96.42	98.66	2.27%
	Δ*p*	331.26	335.64	1.31%
C, TOPSIS	*Nu*	51.93	50.36	3.12%
	Δ*p*	297.81	298.73	0.31%

6. Conclusion

In this paper, the numerical simulations were carried out to explore the heat transfer and flow characteristics of the WPHE with chevron sinusoidal corrugated plates. Parametric analysis based on Fluent software and optimal solutions by means of algorithm both have been investigated. The geometric variables of the plate include the height of the corrugations(*H*), the pitch of the corrugations(*P*) and the chevron angle (*β*). The velocity of the inlet was in the range of 0.1 m/s to 0.5 m/s. The mechanism of heat transfer and flow form in flow channels also had been discussed. The main conclusions could be concluded as follow:

(1) The shape of the flow channel in WPHE could easily change the flow form of the working fluid. Due to outer fluid easily squeezed by the inner fluid and generated a tangential force perpendicular to the direction of the flow channel, the flow form of the outer fluid generally turned to cross flow instead. Thus, the flow rate decreased sharply and secondary flow was also formed easily.
(2) The increase of *H* would enlarge the total heat transfer area and the enhancement of heat transfer could also been improved. According to the results, *Nu* increased by 3.02– 3.71 times when *H* increased from 3 mm to 9 mm, while *f* increased by 1.33– 1.49 times; The *β* mainly affected the number of corrugations and heat transfer area. When $\beta = 30°$, *Nu* reached the maximum and *f* was also the highest than the other two; *P* has the greatest impact on

the structure of flow channel. As P increased, both Nu and f gradually decreased.

(3) Within the range of this paper, the JF factor reached the highest when the height was designed as 9 mm, reaching 0.043.

(4) With the help of ANNs and MOGA, the optimized structure had the best thermal-hydraulic performance under the same working conditions. The maximum JF could be obtained when $P = 15.132$ mm, $H = 3.005$ mm, $\beta = 45.495°$.

CRediT authorship contribution statement

Li Yicong: Conceptualization, Methodology, Software. **Shi Chunyu:** Visualization, Investigation. **Liu Wei:** Supervision, Writing – review & editing. **Liu Zhichun:** Supervision, Writing – review & editing.

Declaration of Competing Interest

The authors declare that they have no known competing financial interests or personal relationships that could have appeared to influence the work reported in this paper.

Data availability

No data was used for the research described in the article.

Acknowledgements

This work was Supported by the National Natural Science Foundation of China (Grant No. 52076088), the National Key Research and Development Program of China (No. 2022YFB4003801) and Core Technology Research Project of Shunde District, Foshan City, China (No. 2130218002932).

References

[2] M.M. Abu-Khader, Plate heat exchangers: recent advances, Renew. Sust. Energ. Rev. 16 (4) (2012) 1883–1891.
[3] B. Sundén, R.M. Manglik, Plate Heat Exchangers: Design, Applications and Performance, Wit Press, 2007.
[4] A. Lozano, F. Barreras, N. Fueyo, S. Santodomingo, The flow in an oil/water plate heat exchanger for the automotive industry, Appl. Therm. Eng. 28 (10) (2008) 1109–1117.
[5] A.G. Kanaris, A.A. Mouza, S.V. Paras, Flow and heat transfer prediction in a corrugated plate heat exchanger using a CFD code, Chemical Engineering & Technology 29 (8) (2006) 923–930.
[6] Y.C. Tsai, F.B. Liu, P.T. Shen, Investigations of the pressure drop and flow distribution in a chevron-type plate heat exchanger, International Communications in Heat and Mass Transfer 36 (2009) 574–578.
[7] S. Jain, A. Joshi, P.K. Bansal, A new approach to numerical simulation of small sized plate heat exchangers with chevron plates, J. Heat Transf. 129 (2007) 291–297.
[8] F.C.C. Galeazzo, R.Y. Miura, J.A.W. Gut, C.C. Tadini, Experimental and numerical heat transfer in a plate heat exchanger, Chem. Eng. Sci. 61 (2006) 7133–7138.
[9] W.W. Focke, The. Effect of the corrugation angle plate heat exchangers[J], International Journal on the Thermohydraulic Performance of Heat Mass Transf. 28 (8) (1985) 1469–1479.
[11] C. Zimmerer, P. Gschwind, Kottke V. Gaiser, Comparison of heat and mass transfer in different heat exchanger geometries with corrugated walls[J], Exp. Thermal Fluid Sci. 26 (2) (2002) 69–273.
[12] T.A. Rush, T.A. Nuwell, A.M. Jacobi, An experimental study of flow and heat transfer in sinusoidal wavy passages[J], Int. J. Heat Mass Transf. 42 (1999) 1541–1553p.
[13] A. Muley, R.M. Manglik, Experimental study of turbulent flow heat transfer and pressure drop in a plate heat exchanger with chevron plates[J], J. Heat Transf. 121 (1) (1999) 110–117.
[14] S.D. Hwang, I.H. Jang, H.H. Cho, Experimental study on flow and local heat mass transfer characteristics inside corrugated duct[J], Int. J. Heat Fluid Flow 17 (1) (2006) 21–32.
[15] D. Dovic, B. Palm, S. Svaic, Generalized correlations for predicting heat transfer and pressure drop in plate heat exchanger channels of arbitrary geometry[J], Int. J. Heat Mass Transf. 51 (19) (2009) 4553–4563.
[16] X. Han, L.Q. Cui, S.J. Chen, et al., A numerical and experimental study of chevron corrugated plate heat exchangers[J], International Communications in Heat and Mass Transfer 37 (8) (2010) 1008–1014.
[17] G. Iulian, G. Nicolas, T.N. Cong, Effects of smooth longitudinal passages and port configuration on the flow and thermal fields in a plate heat exchanger[J], Appl. Therm. Eng. 31 (17) (2011) 4113–4124.
[18] F.B. Liu, Y.C. Tsai, An experimental and numerical investigation of fluid flow in a cross corrugated channel[J], Heat Mass Transf. 46 (5) (2010) 585–593.
[19] W. Roetzel, S.K. Das, X. Luo, Measurement of the heat transfer coefficient in plate heat exchangers using a temperature oscillation technique, Int. J. Heat Mass Transf. 37 (Suppl. 1) (1994), 325e331.
[20] H. Safikhani, S. Eiamsa-ard, Pareto based multi-objective optimization of turbulent heat transfer flow in helically corrugated tubes, Appl. Therm. Eng. 95 (2016) 275–280.
[21] H. Zarea, F.M. Kashkooli, M. Soltani, M. Rezaeian, A novel single and multiobjective optimization approach based on bees algorithm hybrid with particle swarm optimization (BAHPSO): application to thermal-economic design of plate fin heat exchangers, Int. J. Therm. Sci. 129 (2018) 552–564.
[22] P. Ocłon, S. Łopata, T. Stelmach, M. Li, J.-F. Zhang, H. Mzad, W.-Q. Tao, Design optimization of a high-temperature fin-and-tube heat exchanger manifold – a case study, Energy 215 (2021), 119059.
[23] B.S. Mekki, J. Langer, S. Lynch, Genetic algorithm-based topology optimization of heat exchanger fins used in aerospace applications, Int J Heat Mass Tran 170 (2021), 121002.
[24] Dingbiao Wang, Haoran Zhang, Guanghui Wang, Xu Honglin Yuan, Peng., Experimental and numerical study on the heat transfer and flow characteristics of convex plate heat exchanger based on multi-objective optimization, Int. J. Heat Mass Transf. 202 (2023), 123755.
[25] V. Yakhot, S.A. Orszag, Renormalization group analysis of turbulence. I. Basic theory, J. Sci. Comput. 1 (1) (1986) 3–51.
[26] Yicong Li, Zuoqin Qian, Qiang Wang, Numerical investigation of thermohydraulic performance on wake region in finned tube heat exchanger with section-streamlined tube, Case Studies in Thermal Engineering 33 (2022), 101898.
[27] Y. Li, Z. Qian, Q. Wang, Numerical analysis on thermohydraulic performance of the tube inserted with rectangular winglet vortex generators, Energies 15 (2021) 179.
[28] P. Bharadwaj, A. Khondge, A. Date, Heat transfer and pressure drop in a spirally grooved tube with twisted tape insert, Int. J. Heat Mass Transf. 52 (2009) 1938–1944.
[29] R.L. Webb, N.H. Kim, Principle of Enhanced Heat Transfer, second ed., Taylorand Francis Group, New York, 2005.
[30] C.A.C. Coello, G.T. Pulido, M.S. Lechuga, Handling multiple objectives with particle swarm optimization, IEEE Trans. Evol. Comput. 8 (2004) 256–279.
[31] C.-L. Hwang, Y.-J. Lai, T.-Y. Liu, A new approach for multiple objective decision making, Comput. Oper. Res. 20 (1993) 889–899.